

Observation of Edge States in Multilayer WTe₂

Ce Huang^{1,2†}, Awadhesh Narayan^{3†}, Enze Zhang^{1,2}, Shanshan Liu^{1,2}, Changjiang Yi⁴,
Youguo Shi^{4,5}, Stefano Sanvito⁶, Faxian Xiu^{1,2,7*}

¹ State Key Laboratory of Surface Physics and Department of Physics, Fudan University, Shanghai 200433, China

² Collaborative Innovation Center of Advanced Microstructures, Nanjing 210093, China

³ SSCU, Indian Institute of Science, Bengaluru 560012, India

⁴ Institute of Physics and Beijing National Laboratory for Condensed Matter Physics, Chinese Academy of Sciences, Beijing 100190, China

⁵ School of Physical Sciences, University of Chinese Academy of Sciences, Beijing 100190, China

⁶ School of Physics, AMBER and CRANN Institute, Trinity College, Dublin 2, Ireland

⁷ Institute for Nanoelectronic Devices and Quantum Computing, Fudan University, Shanghai 200433, China

[†]These authors contributed equally to this work.

*Correspondence and requests for materials should be addressed to F. X. (E-mail: Faxian@fudan.edu.cn).

Abstract

Three-dimensional (3D) topological semimetals possess unconventional surface and edge states, which play central roles in exotic topological phases. WTe₂, as a type-II Weyl semimetal, has 2D Fermi arcs on the (001) surface in the bulk and 1D helical edge states in its monolayer. These features have recently attracted wide attention in condensed matter physics. However, in the intermediate regime between the bulk and monolayer, the edge states have not been resolved owing to its closed band gap which makes the bulk states dominant. Here, we report the signatures of the edge states by superconducting quantum interference measurements in multilayer WTe₂ Josephson junctions and we directly map the localized supercurrent. In thick WTe₂ (~60 nm), the supercurrent is uniformly distributed on the (001) surface. In thin WTe₂ (10 nm), however, the supercurrent becomes confined to the 1D edge modes and its width reaches up to 1.4 μm. Furthermore, an asymmetric Josephson effect ($|I_c^+(B)| \neq |I_c^-(B)|$), predicted as a unique characteristic of inversion-symmetry-breaking topological systems, is observed in thin WTe₂ whereas it is absent in the thick one. The ability to combine superconductivity with these topological states establishes WTe₂ as a promising topological system with exotic quantum phases and a rich physics of extra dimensionality and tunability.

Introduction

The most fascinating and important phenomena in condensed matter physics emerge from the quantum mechanics of electrons in a lattice, where the periodic potential gives rise to Bloch energy bands. More interestingly, if the Bloch wave functions have a non-trivial topology¹⁻⁴, unconventional boundary states can arise at the lattice edge resulting from the topological discontinuity between the inside and the outside of the material¹. The first such material system to be studied was a 2D topological insulator (TI), in which the 1D helical edge modes give rise to the quantum spin Hall effect⁵. Recently, in 3D topological semimetals (TSM), the broken translational symmetry can also create topological edge/surface states⁶, which have unconventional properties. For example, the 3D quantum Hall effect is realized by Weyl-orbit edge modes in Dirac semimetal Cd_3As_2 ⁷. Therefore, the non-trivial edge states play a central role in exotic topological phases, and thus, the identification of these edge states becomes crucial for elucidating and exploiting topological physics.

Layered WTe_2 was suggested as the first material candidate to be a type-II Weyl semimetal, where eight separated Weyl points exist in the bulk and topological Fermi arcs occur on the (001) crystal surfaces owing to the reflection symmetry⁸. An extra set of quantum oscillations arising from Weyl orbits were observed as evidence of Fermi arcs in transport⁹. Intriguingly, when the thickness is reduced to the monolayer, WTe_2 turns to be a quantum spin Hall insulator with topological edge states, which have been demonstrated in numerous experiments involving low-temperature transport^{10, 11}, angle-resolved photoelectron spectroscopy¹², scanning tunneling microscopy^{13, 14} and microwave impedance microscopy¹⁵. Thus, both 2D surface states and 1D edge modes exist in the WTe_2 system.

While the boundary modes of WTe_2 have been well studied in both the 3D and 2D limits, in multilayers these modes become rather complicated due to the intervening bulk and edge states and thus they remain largely unexplored. Here we have tackled this challenge by performing superconducting quantum interference (SQI) measurements in multilayered WTe_2 Josephson junctions. First, we start with the discussion of the band structures predicted by first-principles calculations for few-layer WTe_2 (see Methods for details). Due to the strong spin-orbit coupling (SOC), the band structure is gapped with a bandgap separating the valence band from the conduction band in monolayer WTe_2 , as shown in Fig. 1a. Helical edge states emerge from the gapped topological non-trivial bulk band structure^{13, 16}. The density of states in the semi-infinite ribbon geometry shown in Fig. 1b clearly display the nontrivial edge states traversing the bulk band gap energy window with a large contribution to the density of states as labeled by the white arrows. Moreover, the edge modes also exist in the bilayer and trilayer WTe_2 as shown in Fig. 1c and Fig. 1d, respectively, while for an increasing number of layers the bulk gap shrinks (also see Fig. S1a-b for bilayer and trilayer band structures). Each layer has one set of topological non-trivial edge modes, and depending on the number of layers the system is either a weak or strong 2D TI associated with an even or odd number of layers, respectively (see Fig. S2 for the calculation of topological invariants). In the thick limit, WTe_2 becomes a Weyl semimetal with Fermi-arc surface states (see Fig. S3 and SI Section I for details). Therefore, the topological boundary states change from the 2D Fermi arcs in the bulk limit to the 1D helical modes in few-

layer WTe₂. It is then interesting to investigate the critical thickness and the evolution of how WTe₂ transforms from a 3D Weyl semimetal to a 2D TI phase.

Unlike the case of 3D TI and monolayer WTe₂ where definitive edge-state signatures can be identified within insulating bulk states, the nearly-closed band gap in multilayer WTe₂ results in a large density of bulk states. Therefore, it is difficult to distinguish the edge states through a gating approach. In order to resolve these edge states in transport measurements, it is then necessary to make them distinct from the coexisting bulk ones. The topological protection makes the boundary states robust and the charge carriers are protected against backscattering, resulting in a high mobility and a long mean free path. However, separating edge and bulk states in a single electrical conductance measurement may be ambiguous. In contrast, if the charge carriers condense together to form Cooper pairs, the difference can be amplified since the supercurrent properties are largely related to the coherence length. Therefore, we have designed a planar microscopic Josephson junction to realize superconducting TSM, which elucidates the topological boundary states. For example, in Nb/Bi₂Te₃/Nb Josephson junctions the surface states enable the ballistic Josephson current rather than the diffusive bulk transport¹⁷. The supercurrent distribution in real space can be also quantitatively extracted from the SQI measurements, where a perpendicular magnetic field induces oscillations in the amplitude of the superconducting current in Josephson junctions. This approach has been widely adopted to reveal the quantum spin Hall edge states in HgTe quantum well¹⁸, topological surface states in TI¹⁹ and quantum Hall edge states in graphene²⁰, but not yet in TSM. And the unique asymmetric Josephson effect, ascribed to the inversion-symmetry-breaking topological systems, has also been anticipated in the WTe₂ system²¹.

Here, we report the observation of edge states in multilayer WTe₂. By varying the thickness of WTe₂ in SQI experiments, we are able to observe the Fraunhofer and SQUID pattern in thick and thin WTe₂, respectively, which indicates the edge superconductivity in thin WTe₂. The 1D edge states exist in multilayer WTe₂ up to 16 nm, while the bulk supercurrent density amplitude is about 1/3 of the edge states in the thinnest sample. An asymmetric Josephson effect is also observed in thin WTe₂ due to the inversion symmetry breaking which further provides the evidence of the edge superconductivity.

WTe₂ Josephson junctions

We first measure several Josephson junctions consisting of WTe₂ flakes of different thicknesses contacted by niobium (Nb) leads. The fabrication and characterization details are described in the Methods and SI Section II (Figs. S4-7). A scanning electron microscopy (SEM) image of the actual device and its measurement configuration are displayed in Fig. 2a (device #1, 10 nm-thick WTe₂). The length and width of the superconducting channel are $L = 200$ nm and $W = 13$ μ m, respectively. Figure 2b shows the resistance-temperature (R - T) curve of the junction with two transitions T_{c1} and T_{c2} at zero magnetic field. $T_{c1} \sim 8$ K originates from the Nb superconducting transition, while $T_{c2(on)} \sim 3$ K comes from the superconducting proximity effect (see SI Section III and Fig. S8 for the Nb superconducting properties). The resistance continues to drop to 10^{-3} times of the normal resistance below

$T_{c2(off)} \sim 1$ K. The tail of the resistance curve, as shown by the green line, can be explained with the Berezinskii–Kosterlitz–Thouless (BKT) transition²² using the Halperin-Nelson equation²³

$$R = R_0 \exp \left\{ -2b \left(\frac{T_{c0} - T}{T - T_{BKT}} \right)^{1/2} \right\}.$$

Here, R_0 and b are material parameters, which designate a zero-Ohmic-resistance state driven by the binding of vortex-antivortex pairs at the BKT transition temperature $T_{BKT} = 0.7$ K, consistent with the voltage-current (V - I) behavior $V \propto I^3$ at 0.7 K (another evidence of the BKT transition, see SI Section IV and Fig. S9 for details). In contrast, a gradual decrease of the junction resistance at the temperature above $T_{c2(on)}$ leads to a broadened superconducting onset, which can be well reproduced by the Aslamazov-Larkin²³ fit (red dashed line) for the 2D conductivity fluctuations. These behaviors are consistent with the expectation for the 2D superconductivity since WTe₂ is in the 2D regime and they are highly reproducible across devices, as shown in SI Fig. S10. Figure 2c and its inset display the I - V characteristics and the differential resistance (dV/dI) of the junction at 45 mK, respectively. From the slope of the I - V curve, the normal-state resistance $R_N \sim 1.7 \Omega$ is extracted. For $|I| < 4.1 \mu\text{A}$, the voltage and dV/dI across the junction remain nearly zero, indicating a robust Josephson effect. Eight WTe₂ Josephson junctions with various L and W are studied (see Table I for their junction parameters), all exhibiting a finite supercurrent at low temperatures with reproducible behavior (SI Section V and Figs. S10-S11). This indicates that the junction is in the long junction limit²⁴ as it also follows the $1/L$ dependence found from the $I_c R_N$ plot versus L in Fig. 2d. In this long junction regime, the critical current is given^{24, 25} by $I_c \sim \frac{E_{Th}}{eR_N}$, being determined by the Thouless energy E_{Th} , which can be estimated²⁶ to be $\sim \hbar v_F/L$, yielding $I_c R_N \propto 1/L$ (see SI Section VI and Fig. S12).

The superconducting quantum interference measurements

Having established the Josephson effect in our Nb/WTe₂/Nb junctions, we then focus on the supercurrent and the edge states of WTe₂. In our experiments, the spatial distribution of the supercurrent is analyzed by applying a perpendicular magnetic field B during the SQI measurements with different thickness of WTe₂. From these, the evidence of the edge states is acquired. In general, the maximum supercurrent that can flow through a Josephson junction is periodically modulated by the magnetic field. Typically, the period of the modulation corresponds to the magnetic flux quantum $\Phi_0 = h/2e$. The particular shape of the critical current interference pattern depends on the phase-sensitive summation of the supercurrents traversing the junction. In the case of a symmetric supercurrent distribution, this integral takes the simple form²⁷:

$$I_c^{max}(B) = \left| \int_{-\infty}^{\infty} J_c(x) \cos \left(\frac{2\pi L_{eff} B x}{\Phi_0} \right) dx \right|$$

where L_{eff} is the effective length of the junction along the direction of the current, accounting for the magnetic flux threading²⁸ through parts of the superconducting contacts over the London penetration depths.

Firstly, we apply the magnetic field along the z -axis as shown schematically in Fig. 3a. In thick WTe₂, the bulk states dominate and along the y -axis the supercurrent density

has an approximately uniform distribution. Thus, the uniform current density yields the single-slit Fraunhofer pattern described by²⁷

$$I_c(B) = I_{c0} \left| \sin \left(\frac{\pi L_{eff} B W}{\Phi_0} \right) / \left(\frac{\pi L_{eff} B W}{\Phi_0} \right) \right|.$$

We have measured device #8 with 60 nm-thick WTe₂ as shown in Fig. 3b. The critical current envelope has an oscillation characteristic. We obtain a period of ~ 0.33 mT, which yields the effective length of $L_{eff} = \Phi_0 / (\delta B_{lobe} W) \sim 1.0$ μm . This effective length, larger than the distance between the two Nb electrodes ($L = 240$ nm), is caused by the London penetration depth and the flux focusing due to the Meissner effect^{29, 30}. The critical current envelope strongly resembles a single-slit pattern with $2\Phi_0$ central lobe width. The corresponding supercurrent distribution is obtained by transforming the single-slit pattern to the real-space current density, $J_c(z)$, as shown in Fig. 3c. This suggests a nearly uniform supercurrent density throughout the y direction. The full details of the extraction procedure can be found in the SI section VII and Fig. S13. Furthermore, the critical currents overlap each other at different current directions as shown in Fig. 3d which indicates a conventional Josephson effect with $|I_c^+(B)| = |I_c^-(B)|$, where $+$ and $-$ denote the sweep direction of the bias current and $+B$ and $-B$ are the magnetic field directions.

Next, we examine thinner WTe₂ Josephson junctions. When the WTe₂ is thinned down to a few layers, the 1D counter-propagating helical modes are developed at the edges as numerically simulated in Fig. 1b-d. The low bulk density of states coexists with the high-density edge states as shown in Fig. 3e. The magnetic-field-dependent critical current envelope in a 13 nm-thick WTe₂ device (device #2) demonstrates the Φ_0 periodic SQI (Fig. 3f). I_c decays slowly which is distinct from Fraunhofer pattern in Fig. 3b. We use an edge-stepped nonuniform supercurrent model to directly simulate the $I_c - B$ relation as shown by the black line in Fig. 3f (see the model details in SI Section VIII and Fig. S14). The good fit of both the magnitude and periodicity of I_c indicates the nonuniform supercurrent and robust edge channels in few-layer WTe₂. Furthermore, the SQUID-like interference pattern corresponds to the development of sharp peaks in the supercurrent density at the mesa edges in Fig. 3g. The widths of the supercurrent-carrying edge channels are estimated to be in the range 1.3 – 1.4 μm . The relation of the critical current with the magnetic field is presented in Fig. 3h.

The critical currents are observed to follow $|I_c^+(B)| \neq |I_c^-(B)|$. This is consistent with the predicted effect of inversion-symmetry-breaking on Weyl semimetal²¹. In general, the total Josephson current carried by the two edge states can be described by³¹

$$I(\Phi, \varphi) \propto I_1 \sin(n\varphi + n\Phi) + I_2 \sin(n\varphi - n\Phi)$$

where I_1 and I_2 represents the Josephson current carried by the two edges, Φ and φ are the phase in WTe₂ (magnetic field related) and Nb regions (current related), respectively. In thick WTe₂, the bulk dominated channels will have $I_1 = I_2$ and Josephson current can be written as $I(\Phi, \varphi) \propto (I_1 + I_2) \cos(n\Phi) \sin(n\varphi)$ which gives a symmetric critical current with respect to the signs of the magnetic field. However, the two edges have different energy spectra and $I_1 \neq I_2$ in thin WTe₂ which results from different Fermi velocity of the two edge sides, denoted by the red and blue

lines as shown in Fig. 3e. Therefore, the $I(\Phi, \varphi)$ is not symmetric for both φ and Φ anymore. We also note that in several low magnetic fields, the critical current shows a peculiar symmetry relation with the magnetic field, such as $I_c^+(0.26 \text{ T}) \approx I_c^-(-0.26 \text{ T})$ due to the time-reversal invariant²¹ which has been reported in 2D TI HgTe Josephson junction³² with helical edge states.

We have reproduced the edge mode superconductivity and the SQUID-like pattern in 10 nm-thick WTe₂ device (#1), and the traditional Fraunhofer pattern in a 40 nm-thick WTe₂ device (#5, see SI Section IX and Fig. S15 for details). The higher supercurrent density carried by the edge states suggests a robust coupling to the superconductor electrodes. To further distinguish the superconducting proximity effect of edge/bulk channels, we perform the experiment in a 16 nm-thick WTe₂ device (#3) to distinguish the bulk and edge superconductivity. Two groups of Josephson junctions are edge-crossing (R_1) and edge-untouched (R_2) as shown in Fig. 4a. For R_2 , the junction is easier to be conducted by the bulk states because the electrodes are closer in the central region ($L_b \sim 0.4 \mu\text{m}$) while far at the edge. The distance on the edge side is $L_s \sim 4 \mu\text{m}$ that makes it hard to realize the Josephson effect through the edge channels. Since the thickness is uniform in this sample, as indicated by the atomic force microscopy (AFM) measurement (Fig. S6), we can reasonably assume that the junction resistance is isotropic and inversely proportional to the width. Figure 4b shows the R - T curve at low temperatures. The normal-state resistance is $R_{1N} \sim 1.5 \Omega$ and $R_{2N} \sim 17.5 \Omega$. The channel width of R_1 is 8 times to that of R_2 from the SEM image. The eight times of R_1 is still smaller than R_2 indicating the higher conductivity at edges. Moreover, only edge-crossing R_1 can reach zero to exhibit Josephson effect while R_2 only decreases a little. The differential resistance versus the current measurement in Fig. 4c verifies this property. Since the lengths of two junctions differ slightly, the coherence length of R_1 should be larger than that of R_2 to realize the Josephson effect. A similar SQUID pattern with edge-dominated supercurrent is also observed, as shown in Fig. S15b, which is consistent with the other two thin devices (#1 and #2).

We further change the magnetic field direction to be in-plane to measure the supercurrent distribution along the z -axis. A mixture of Fraunhofer and SQUID-like pattern is observed in the SQI experiment (see SI section IX and Fig. S16 for details). The supercurrent flows along the top and bottom surfaces with a higher density which indicates surface superconductivity possibly arising from the Fermi-arc states.

Discussion

It is necessary to distinguish whether the observed edge superconductivity originates from the edge states in WTe₂ or other effects. In graphene, “fibre-optic” modes exist at the edge due to the band bending³³. This trivial effect will also result in the SQUID interference pattern³³. However, this edge-mode-dominated current flow can be observed only near the Dirac point, not at a higher density of states. The conductance of thin WTe₂ is larger than the quantum conductance ($t \cdot \frac{2e^2}{h}$, t is the thickness) indicating a non-negligible bulk contribution and a high Fermi level. Moreover, all the three different devices exhibit the sharp edge states which further excludes the accidental impurity effect. The asymmetric Josephson effect we observed

in Fig. 3g also shows consistent signatures with the topological edge states due to the inversion symmetry breaking. Thus, these results provide the evidence of strong edge states in multilayer WTe₂.

We summarize the supercurrent amplitude of the surface states and edge states in Fig. 5. Surface states are more evident in thick devices, while the edge modes gradually emerge in thinner ones. The edge/bulk supercurrent amplitude reaches 2.76 in 10 nm-thick WTe₂. At the same time, each edge/bulk channel length ratio is ~ 0.07 in Fig. S14b. Supposing the conductivity from edge and bulk is the same, the conductance is inversely proportional to the channel length, and the conductance contribution is assumed to be $\frac{G_{edge}}{G_{bulk}} \sim \frac{1.8 \mu\text{m}}{13 \mu\text{m}} \sim 0.14$. Thus, the total conductance, $G = G_{edge} + G_{bulk}$, will be dominated by the bulk contribution, making it difficult to distinguish the edge states through the transport measurement. Therefore, our superconducting Josephson junction method can detect the weak edge modes in multilayer WTe₂, where the bulk states cannot be neglected. The critical thickness for the transition from 1D edge modes to 2D surface modes is estimated to be $t_c = 16 - 20$ nm. Within this range, both 1D and 2D modes coexist. Moreover, various topological semimetals such as the TaAs family³⁴ (Fermi-arc surface states), layered MoTe₂³⁵ (edge states in the 2D limit) and ZrSiS³⁶ (nodal-line surface states) can be further fabricated into Josephson junctions to detect the surface/edge states.

In summary, by studying the Fraunhofer interference, our measurements provide the supercurrent distribution in type-II Weyl semimetal WTe₂. In thick WTe₂, the supercurrent is found to be carried more by the surface states. In thin WTe₂, however, the existence of edge channels is evidenced. Such supercurrent distributions additionally provide a direct measurement of the edges states' spatial extension. Besides, the unusual asymmetric Josephson effect in WTe₂ through the edge channels is an intrinsic property of the inversion symmetry breaking and different Fermi velocity of edge states, which is distinct from other systems by an external in-plane magnetic field²⁸. Furthermore, the Josephson junctions formed from 1D or 2D edge states and *s*-wave superconducting contacts are expected to emulate spinless *p*-wave superconductivity³⁷ and Majorana flat bands³⁸ at 1D and 2D edge, respectively, via *a.c.* Josephson effect by Shapiro response measurements. Josephson supercurrents through the helical edge channels and surface states establish WTe₂ as a promising platform for the future realization of topological superconductivity and Majorana bound states.

Methods

WTe₂ crystal growth

High-quality bulk WTe₂ crystals were grown by chemical vapor transport (CVT) method as reported before³⁹. Single crystals of WTe₂ were grown by a high-temperature self-flux method. High-purity tungsten powders (99.9%) and Te pieces (99.999%) were inserted into alumina crucibles with a molar ratio of 1:30 in a glove box filled with pure argon then sealed in quartz tubes under high vacuum. The tubes were heated to 1100 °C in 20 hours and maintained for 10 hours. Then the furnace was slowly cooled down to 650 °C with a rate of 2 °C/h followed by separating the Te flux in a centrifuge at 650 °C.

Device fabrication

The WTe₂ flakes were mechanically exfoliated onto a Si substrate capped with a 280 nm-thick SiO₂ layer and the thickness of WTe₂ was identified by optical contrast and atomic force microscopy. The WTe₂ Josephson junctions were fabricated by an *e*-beam lithography technique and wet-etched by standard buffered HF solution for 5 s in the electrode regime. We deposited 120 nm-thick Nb electrodes using magnetic sputtering. Then, 40 nm-thick SiO₂ was deposited on top to prevent the WTe₂ oxidization.

Transport measurements

Four-terminal temperature-dependent transport measurements were carried out in a Physical Property Measurement System (PPMS, Quantum Design) with a dilution refrigerator, which achieves a base temperature of 35 mK. The transport properties were acquired using lock-in amplifiers (SR830) and Agilent 2912 meters. To probe the superconducting proximity, we used an excitation current of <50 nA. In differential resistance (dV/dI) measurements, a small *a.c.* current bias (10 nA to 100 nA) is generated by the lock-in amplifier output voltage in combination with a 10 M Ω bias resistor. This small *a.c.* current is added on top of the larger *d.c.* current bias by Agilent 2912, and the induced differential voltage is measured using the lock-in technique with a low frequency (<50 Hz).

First-principles calculations for WTe₂ band structure

First-principles calculations were carried out using the Vienna Ab-initio Simulation Package (VASP)⁴⁰. The Perdew-Burke-Ernzerhof parametrization of the exchange-correlation functional was employed⁴¹. A plane wave cut-off of 300 eV and an $8 \times 12 \times 4$ *k*-point mesh were used for the bulk structure. For the slab calculations, a corresponding $8 \times 12 \times 1$ *k*-point grid was chosen, with at least 15 Angstroms of vacuum separating periodic images. By computing the maximally localized Wannier functions of WTe₂, a tight-binding model was derived using the W 5d and 6s states, and the Te 5s and 5p states⁴². The WannierTools code was then employed to analyze the surface and edge state properties⁴³.

Figures and Captions

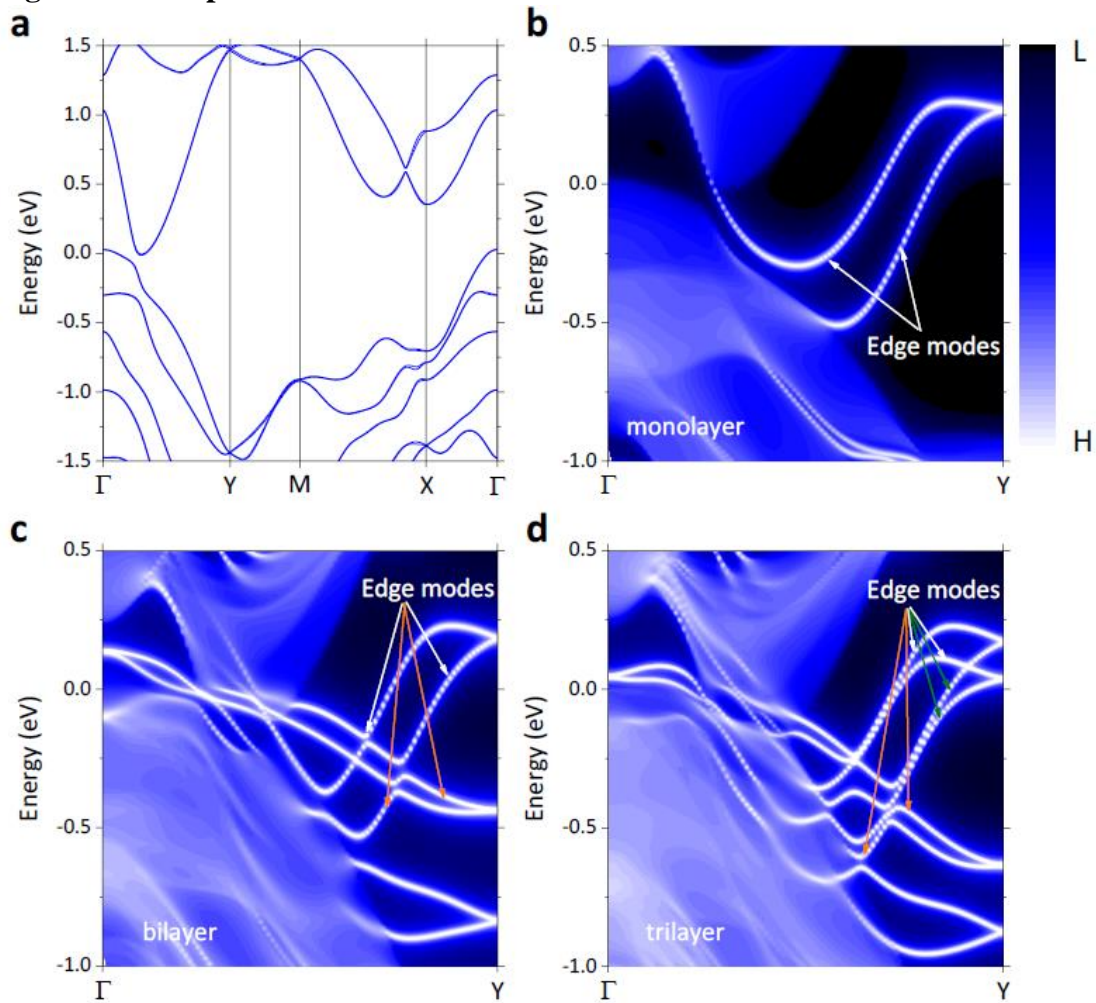


Figure 1 | Band structure and calculated topological states of WTe_2 . (a) The band structures of monolayer WTe_2 with periodic boundary conditions. (b-d) First-principles calculations on the density of states along $\Gamma - \text{Y}$ in the semi-infinite ribbon geometry for monolayer, bilayer and trilayer WTe_2 , respectively. The edge states span the bulk band gap in monolayer WTe_2 , while the band gap shrinks in bilayer and trilayer WTe_2 . The value of the density of states is plotted by the color scale indicator at the right of Fig. 1b. Each set of edge modes is marked by the arrows in different colors.

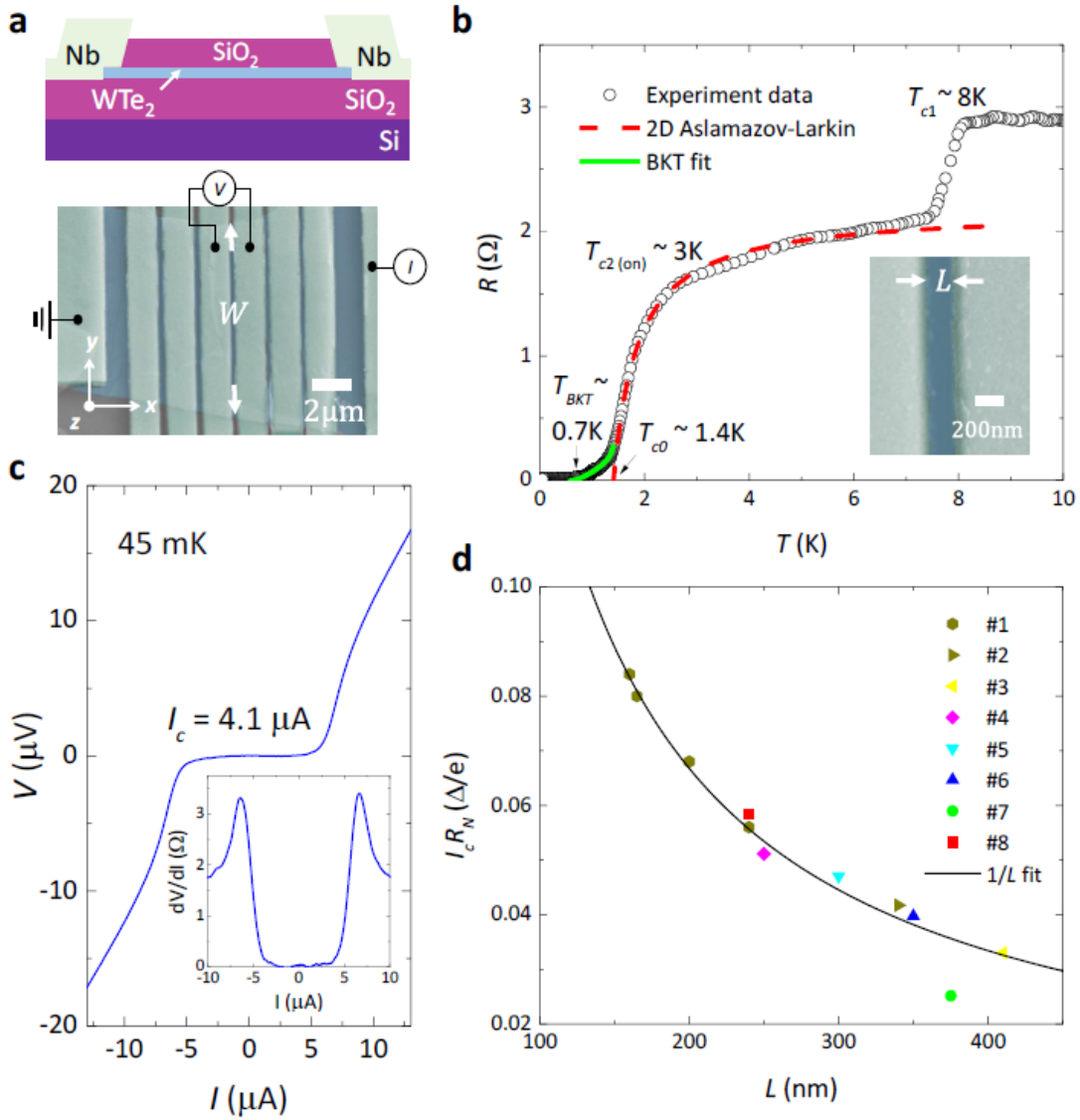


Figure 2 | Josephson effect in thin WTe₂. (a) Top: Junctions schematic. Bottom: False-colour SEM image of the device with the measurement configuration. 120 nm-thick Nb is deposited on the top of WTe₂ (device #1). A four-terminal measurement across the interface was performed. (b) Temperature dependence of WTe₂ Josephson junction resistance. Two transitions are identified: $T_{c1} = 8\text{ K}$ is from the superconducting Nb, $T_{c2(\text{on})} \sim 3\text{ K}$ is from the emergence of superconducting WTe₂ and the supercurrent is identified at $T_{c2(\text{off})} \sim 1\text{ K}$. The red dashed line represents the superconducting amplitude fluctuation taking into account the 2D Aslamazov-Larkin model, which gives the temperature $T_{c0} = 1.4\text{ K}$, at which the finite amplitude of the order parameter develops. The green solid line represents the BKT transition using the Halperin-Nelson equation which yields a BKT transition temperature $T_{\text{BKT}} = 0.7\text{ K}$. Inset shows that the junction has a length of $L = 200\text{ nm}$. (c) I - V characteristics for Josephson junction in the superconducting states with a critical current of $I_c \sim 4.1\ \mu\text{A}$ under zero magnetic field at 45 mK. Inset: dV/dI characteristics indicate zero resistance below the critical current, the same as the I - V curve. (d) Effect of the junction length on supercurrent for eight devices. The product $I_c R_N$ follows a general trend of $I_c R_N \propto 1/L$.

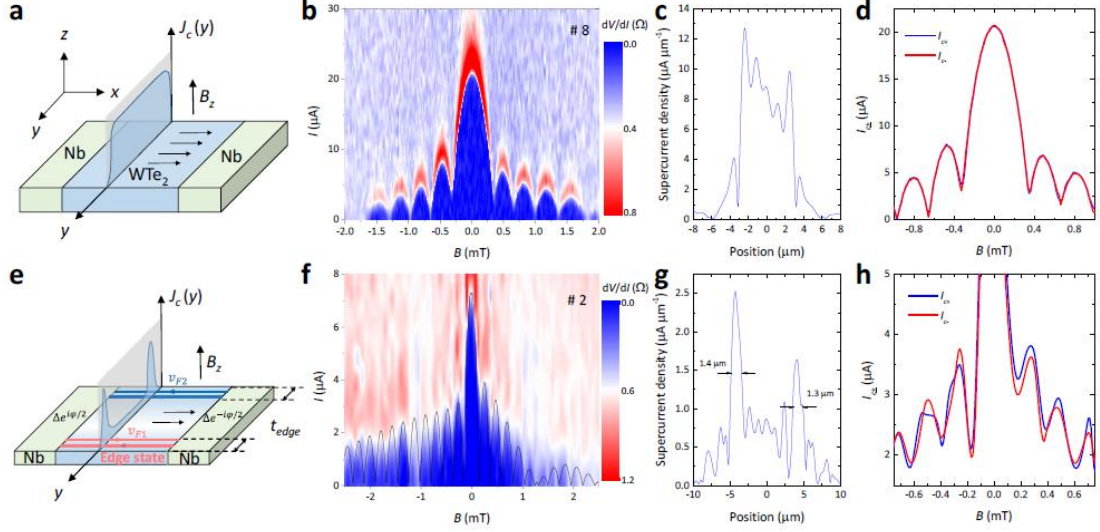


Figure 3 | Evolution of edge superconductivity in thin WTe₂. (a) A schematic picture of a lateral Josephson junction with the out-of-plane magnetic field in thick WTe₂. The thick WTe₂ is filled with charge carriers and the supercurrent can flow uniformly across the junction along the y-axis, corresponding to a flat supercurrent density $J_c(y)$. (b) The differential resistance at different values of B_z in 60 nm-thick WTe₂ (device #8), showing the single-slit interference characteristics with a uniform supercurrent density. (c) The supercurrent distribution along the y-axis, which is calculated by the inverse Fourier transform of the data in (b). The supercurrent density is uniform along the y-axis, consistent with trivial bulk charge transport. (d) Critical current I_c as a function of B for the two sweep directions (positive as the blue line, negative as the red line). Two curves overlap with each other. (e) A schematic picture of a lateral Josephson junction with the out-of-plane magnetic field where $\Delta e^{\pm i\varphi/2}$ denotes the pairing order parameter of two superconducting Nb electrodes. In thin WTe₂, the bulk domination decreases and the supercurrent is carried by the helical edge states. The edge states on two sides of WTe₂ have different Fermi velocities v_{F1} and v_{F2} when the inversion symmetry is broken that gives rise to the asymmetric Josephson effect. (f) Differential resistance across the 13 nm-thick WTe₂ junction (device #2), showing a mixture of Fraunhofer and SQUID-like pattern with a central lobe of width $< 2\Phi_0$ and side lobes of width Φ_0 . The black line shows the fitting results from the edge-stepped supercurrent model. (g) The supercurrent distribution of device #2. The widths of the supercurrent-carrying edge channels are estimated to be 1.3 – 1.4 μm . (h) Critical current I_c as a function of B for the two sweep directions (positive as the blue line, negative as the red line), indicating asymmetric I_c relation.

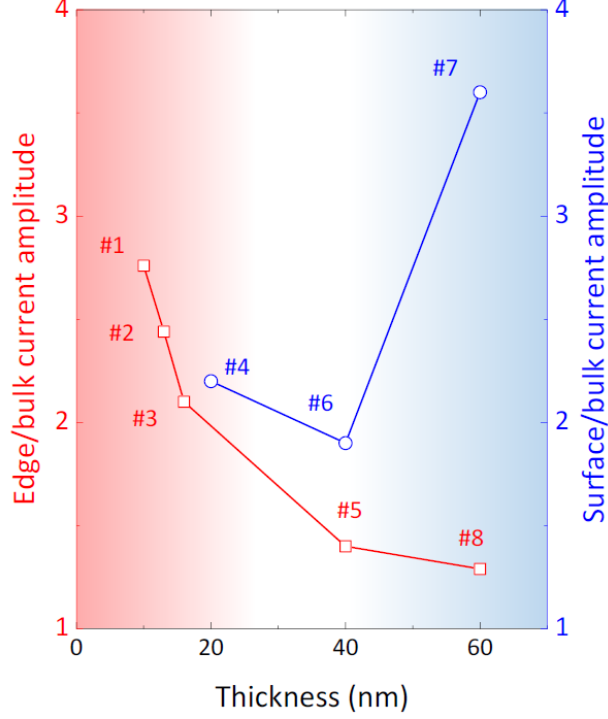


Figure 5 | Summary of thickness-dependent edge and surface contribution in WTe₂. Left and right axis display the edge/bulk and surface/bulk supercurrent amplitude in different thickness WTe₂, respectively. The gradient background represents the supercurrent contribution origin, red for edge states and blue for surface states.

Table 1 Parameters of all junctions.								
Device	t (nm)	L (nm)	W (μm)	R_N (Ω)	I_c (μA)	T_c (K)	Δ_i (μeV)	ξ_N (nm)
#1	10	200	13	1.8	4.1	0.72	108	480
#2	13	340	9	1.0	5.0	0.80	120	440
#3	16	410	13	1.5	2.0	0.60	90	580
#4	20	250	13	2.3	3.0	0.9	135	390
#5	40	300	6	0.35	19	0.92	138	300
#6	40	350	6.5	2.3	1.5	0.58	87	480
#7	60	375	4.5	0.61	6.8	1.1	165	250
#8	60	240	6	0.35	20	0.80	120	340

The thickness t is measured by AFM. The length L and width W are obtained through SEM and Optical microscopy. The normal resistance R_N , critical current I_c , transition temperature T_c can be extracted from the R - T and I - V curves. The superconducting gap and coherence length are estimated by $\Delta_i = 1.76k_B T_c$ and $\xi_N = \frac{\hbar v_F}{\pi \Delta}$, respectively.

References

1. Hasan MZ, Kane CL. Colloquium: Topological insulators. *Rev Mod Phys* 2010, **82**(4): 3045-3067.
2. Young SM, Zaheer S, Teo JCY, Kane CL, Mele EJ, Rappe AM. Dirac Semimetal in Three Dimensions. *Phys Rev Lett* 2012, **108**(14): 140405.

3. Bansil A, Lin H, Das T. Colloquium: Topological band theory. *Rev Mod Phys* 2016, **88**(2): 021004.
4. Armitage NP, Mele EJ, Vishwanath A. Weyl and Dirac semimetals in three-dimensional solids. *Rev Mod Phys* 2018, **90**(1): 015001.
5. König M, Wiedmann S, Brüne C, Roth A, Buhmann H, Molenkamp LW, *et al.* Quantum Spin Hall Insulator State in HgTe Quantum Wells. *Science* 2007, **318**(5851): 766.
6. Wan X, Turner AM, Vishwanath A, Savrasov SY. Topological semimetal and Fermi-arc surface states in the electronic structure of pyrochlore iridates. *Phys Rev B* 2011, **83**(20): 205101.
7. Zhang C, Zhang Y, Yuan X, Lu S, Zhang J, Narayan A, *et al.* Quantum Hall effect based on Weyl orbits in Cd₃As₂. *Nature* 2019, **565**(7739): 331-336.
8. Soluyanov AA, Gresch D, Wang Z, Wu Q, Troyer M, Dai X, *et al.* Type-II Weyl semimetals. *Nature* 2015, **527**: 495.
9. Li P, Wen Y, He X, Zhang Q, Xia C, Yu Z-M, *et al.* Evidence for topological type-II Weyl semimetal WTe₂. *Nat Commun* 2017, **8**(1): 2150.
10. Fei Z, Palomaki T, Wu S, Zhao W, Cai X, Sun B, *et al.* Edge conduction in monolayer WTe₂. *Nat Phys* 2017, **13**: 677.
11. Wu S, Fatemi V, Gibson QD, Watanabe K, Taniguchi T, Cava RJ, *et al.* Observation of the quantum spin Hall effect up to 100 kelvin in a monolayer crystal. *Science* 2018, **359**(6371): 76.
12. Xu S-Y, Belopolski I, Alidoust N, Neupane M, Bian G, Zhang C, *et al.* Discovery of a Weyl Fermion Semimetal and Topological Fermi Arcs. *Science* 2015, **349**(6248): 613.
13. Tang S, Zhang C, Wong D, Pedramrazi Z, Tsai H-Z, Jia C, *et al.* Quantum spin Hall state in monolayer 1T'-WTe₂. *Nat Phys* 2017, **13**: 683.
14. Collins JL, Tadich A, Wu W, Gomes LC, Rodrigues JNB, Liu C, *et al.* Electric-field-tuned topological phase transition in ultrathin Na₃Bi. *Nature* 2018, **564**(7736): 390-394.
15. Shi Y, Kahn J, Niu B, Fei Z, Sun B, Cai X, *et al.* Imaging quantum spin Hall edges in monolayer WTe₂. *Sci Adv* 2019, **5**(2): eaat8799.
16. Qian X, Liu J, Fu L, Li J. Quantum spin Hall effect in two-dimensional transition metal dichalcogenides. *Science* 2014, **346**(6215): 1344.
17. Veldhorst M, Snelder M, Hoek M, Gang T, Guduru VK, Wang XL, *et al.* Josephson supercurrent through a topological insulator surface state. *Nat Mater* 2012, **11**: 417.
18. Hart S, Ren H, Wagner T, Leubner P, Mühlbauer M, Brüne C, *et al.* Induced superconductivity in the quantum spin Hall edge. *Nat Phys* 2014, **10**: 638.
19. Lee JH, Lee G-H, Park J, Lee J, Nam S-G, Shin Y-S, *et al.* Local and Nonlocal Fraunhofer-like Pattern from an Edge-Stepped Topological Surface Josephson Current Distribution. *Nano Lett* 2014, **14**(9): 5029-5034.
20. Amet F, Ke CT, Borzenets IV, Wang J, Watanabe K, Taniguchi T, *et al.* Supercurrent in the quantum Hall regime. *Science* 2016, **352**(6288): 966.
21. Chen C, He JJ, Ali MN, Lee G-H, Fong KC, Law KT. Asymmetric Josephson effect in inversion symmetry breaking topological materials. *Phys Rev B* 2018, **98**(7): 075430.
22. Reyren N, Thiel S, Cavaglia AD, Kourkoutis LF, Hammerl G, Richter C, *et al.* Superconducting Interfaces Between Insulating Oxides. *Science* 2007, **317**(5842): 1196.
23. Saito Y, Kasahara Y, Ye J, Iwasa Y, Nojima T. Metallic ground state in an ion-gated two-dimensional superconductor. *Science* 2015, **350**(6259): 409-413.
24. Dubos P, Courtois H, Pannetier B, Wilhelm FK, Zaikin AD, Schön G. Josephson critical current

- in a long mesoscopic S-N-S junction. *Phys Rev B* 2001, **63**(6): 064502.
25. Ben Shalom M, Zhu MJ, Fal'ko VI, Mishchenko A, Kretinin AV, Novoselov KS, *et al.* Quantum oscillations of the critical current and high-field superconducting proximity in ballistic graphene. *Nat Phys* 2015, **12**: 318.
 26. Ishii C. Josephson Currents through Junctions with Normal Metal Barriers. *Progress of Theoretical Physics* 1970, **44**(6): 1525-1547.
 27. Tinkham M. *Introduction to superconductivity*. McGraw-Hill: New York, 1975.
 28. Suominen HJ, Danon J, Kjaergaard M, Flensberg K, Shabani J, Palmstrøm CJ, *et al.* Anomalous Fraunhofer interference in epitaxial superconductor-semiconductor Josephson junctions. *Phys Rev B* 2017, **95**(3): 035307.
 29. Paajaste J, Amado M, Roddaro S, Bergeret FS, Ercolani D, Sorba L, *et al.* Pb/InAs Nanowire Josephson Junction with High Critical Current and Magnetic Flux Focusing. *Nano Lett* 2015, **15**(3): 1803-1808.
 30. de Vries FK, Timmerman T, Ostroukh VP, van Veen J, Beukman AJA, Qu F, *et al.* h/e Superconducting Quantum Interference through Trivial Edge States in InAs. *Phys Rev Lett* 2018, **120**(4): 047702.
 31. Asano Y, Tanaka Y, Sigrist M, Kashiwaya S. Josephson current in s-wave-superconductor Sr₂RuO₄ junctions. *Phys Rev B* 2003, **67**(18): 184505.
 32. Bocquillon E, Deacon RS, Wiedenmann J, Leubner P, Klapwijk TM, Brüne C, *et al.* Gapless Andreev bound states in the quantum spin Hall insulator HgTe. *Nat Nanotechnol* 2016, **12**: 137.
 33. Allen MT, Shtanko O, Fulga IC, Akhmerov AR, Watanabe K, Taniguchi T, *et al.* Spatially resolved edge currents and guided-wave electronic states in graphene. *Nat Phys* 2015, **12**: 128.
 34. Lv BQ, Xu N, Weng HM, Ma JZ, Richard P, Huang XC, *et al.* Observation of Weyl nodes in TaAs. *Nat Phys* 2015, **11**: 724.
 35. Deng K, Wan G, Deng P, Zhang K, Ding S, Wang E, *et al.* Experimental observation of topological Fermi arcs in type-II Weyl semimetal MoTe₂. *Nat Phys* 2016, **12**: 1105.
 36. Liu J, Balents L. Correlation effects and quantum oscillations in topological nodal-loop semimetals. *Phys Rev B* 2017, **95**(7): 075426.
 37. Fu L, Kane CL. Josephson current and noise at a superconductor/quantum-spin-Hall-insulator/superconductor junction. *Phys Rev B* 2009, **79**(16): 161408.
 38. Chen A, Pikulin DI, Franz M. Josephson current signatures of Majorana flat bands on the surface of time-reversal-invariant Weyl and Dirac semimetals. *Phys Rev B* 2017, **95**(17): 174505.
 39. Huang C, Narayan A, Zhang E, Liu Y, Yan X, Wang J, *et al.* Inducing Strong Superconductivity in WTe₂ by a Proximity Effect. *ACS Nano* 2018, **12**(7): 7185-7196.
 40. Kresse G, Furthmüller J. Efficiency of ab-initio total energy calculations for metals and semiconductors using a plane-wave basis set. *Computational Materials Science* 1996, **6**(1): 15-50.
 41. Perdew JP, Burke K, Ernzerhof M. Generalized Gradient Approximation Made Simple. *Phys Rev Lett* 1996, **77**(18): 3865-3868.
 42. Mostofi AA, Yates JR, Lee Y-S, Souza I, Vanderbilt D, Marzari N. wannier90: A tool for obtaining maximally-localised Wannier functions. *Computer Physics Communications* 2008, **178**(9): 685-699.
 43. Wu Q, Zhang S, Song H-F, Troyer M, Soluyanov AA. WannierTools: An open-source software

package for novel topological materials. *Computer Physics Communications* 2018, **224**: 405-416.